Bioactive Materials 6 (2021) 1853–1866

Contents lists available at ScienceDirect

Bioactive Materials

journal homepage: www.sciencedirect.com/journal/bioactive-materials

A trilogy antimicrobial strategy for multiple infections of orthopedic implants throughout their life cycle

Yikai Wang [a], Wangsiyuan Teng [a], Zengjie Zhang [a], Xingzhi Zhou [a], Yuxiao Ye [c], Peng Lin [a], An Liu [a], Yan Wu [a], Binghao Li [a], Chongda Zhang [d], Xianyan Yang [b], Weixu Li [a], Xiaohua Yu [a,***], Zhongru Gou [b,**], Zhaoming Ye [a,*]

[a] Department of Orthopedics, Centre for Orthopaedic Research, Orthopedics Research Institute of Zhejiang University, The Second Affiliated Hospital, Zhejiang University School of Medicine, Hangzhou 310000, PR China
[b] Bio-nanomaterials and Regenerative Medicine Research Division, Zhejiang-California International Nanosystem Institute, Zhejiang University, Hangzhou 310058, PR China
[c] School of Material Science and Engineering, University of New South Wales, Sydney 2052, Australia
[d] New York University Medical Center, New York University, New York, 10016, USA

ARTICLE INFO

Keywords:
Antibacterial properties
Zinc
Orthopedic implant
Biomimetic apatite mineral
Multifunctional coating

ABSTRACT

Bacteria-associated infection represents one of the major threats for orthopedic implants failure during their life cycles. However, ordinary antimicrobial treatments usually failed to combat multiple waves of infections during arthroplasty and prosthesis revisions etc. As these incidents could easily introduce new microbial pathogens in/onto the implants. Herein, we demonstrate that an antimicrobial trilogy strategy incorporating a sophisticated multilayered coating system leveraging multiple ion exchange mechanisms and fine nanotopography tuning, could effectively eradicate bacterial infection at various stages of implantation. Early stage bacteriostatic effect was realized via nano-topological structure of top mineral coating. Antibacterial effect at intermediate stage was mediated by sustained release of zinc ions from doped CaP coating. Strong antibacterial potency was validated at 4 weeks post implantation via an implanted model *in vivo*. Finally, the underlying zinc titanate fiber network enabled a long-term contact and release effect of residual zinc, which maintained a strong antibacterial ability against both *Staphylococcus aureus* and *Escherichia coli* even after the removal of top layer coating. Moreover, sustained release of Sr^{2+} and Zn^{2+} during CaP coating degradation substantially promoted implant osseointegration even under an infectious environment by showing more peri-implant new bone formation and substantially improved bone-implant bonding strength.

1. Introduction

Infection is one of the most serious complications after elective orthopedic surgery [1]. For example, about 1% of patients develop prosthetic joint infection (PJI) during joint replacement recovery, which cause enormous pain to patients and often lead to implant failures [2]. The root cause of PJI is originated from bacteria residing at the surgical sites or brought in through blood circulation, which can develop into biofilm on implant surface and act as a shield for bacteria [3,4]. Indeed, bacterial biofilm has proved to be able to withstand host immune responses and environmental stress and weaken the therapeutic effects of antibiotics in body [5,6]. Although two-stage revision procedures are still considered as the standard of care for treating prosthetic infections [7], it has been severely suffered from high mortality risk [8], significant functional impairment [9], increased cost, etc. Many efforts have been made in order to develop a one-stage revision procedure which circumvents the shortages of two-stage revision [10–13]. While some of these strategies offer excellent antibacterial properties at early stage of

* Corresponding author. Department of Orthopedics, the Second Affiliated Hospital, Zhejiang University School of Medicine, 88# Jiefang Road, Hangzhou, Zhejiang 310009, PR China.
** Corresponding author. Zhejiang-California International Nanosystems Institute Zhejiang University, Hangzhou 310058, China.
*** Corresponding author. Department of Orthopedics, the Second Affiliated Hospital, Zhejiang University School of Medicine, 88# Jiefang Road, Hangzhou, Zhejiang 310009, PR China.
E-mail addresses: xiaohua.yu@zju.edu.cn (X. Yu), zhrgou@zju.edu.cn (Z. Gou), yezhaoming@zju.edu.cn (Z. Ye).

https://doi.org/10.1016/j.bioactmat.2020.11.030
Received 13 October 2020; Received in revised form 20 November 2020; Accepted 27 November 2020

implantation [14], infections can occur at any stages of joint replacement recovery course [7,15], which largely invalidate the feasibility of these options in clinic. Given this context, it is highly desirable to develop orthopedic implants capable of sustaining their antibacterial properties covering their life cycle.

Titanium alloys (Ti6Al4V) are widely used in the field of orthopedics because of their excellent biocompatibility, moderate elastic module, great corrosion resistance and outstanding osseointegration ability [16–18]. The preparation of ion-doped calcium phosphate (CaP) coating on the surface of titanium alloy has been widely used in the field of orthopedics, achieving great success due to their excellent osseointegration and customizable antibacterial properties [19–21]. However, few of these CaP coatings obtained long-lasting antimicrobial performance. The field of antimicrobial technology has dramatically evolved in the past three decades from systemic antibiotics administration to local diffusion-based antibiotic-eluting strategies [22,23]. Incorporation of antibiotics into medical devices can lead to sustained release of antibiotics and maintain sufficient local antibiotic concentration to combat infection. For example, antibiotic loaded bone cements have been widely used in clinic to prevent orthopedic implant infections and showed tremendous successes [24,25]. However, the release periods of these devices were usually limited up to one month upon implantation, which was largely due to their affinity-based or diffusion-based loading mechanisms. Besides, many of these drug-eluting devices suffer from "initial burst" issue, causing majority of the loaded antibiotics to be released within a very short time period once implanted, which substantially sacrificed the efficacy of these treatments. Thus, there is a need for alternatives to circumvent the short life cycle of antibiotic-eluting devices and offer long-lasting antibacterial potency for implants.

In response to the drawbacks found in antibiotic-eluting approaches, intrinsic antibacterial properties of certain types of materials have attracted more and more attention from research community. Among them, metal ions have been widely used in the antibacterial field due to their intrinsic capability to deactivate respiratory enzyme, interfere DNA replication, and destruct cell membrane [26–28]. Moreover, unlike antibiotics, many of these agents are much less likely to induce bacterial resistance, which readily avoid the risk associated with antibiotic abuse. In particular, as a broad-spectrum antibacterial agent, zinc has been extensively used to prevent microbial infection caused by various bacterial strains such as methicillin-resistant staphylococcus aureus(MRSA) [29]. Kai Y et al. utilized the metal organic framework materials to load zinc components on the surface of the titanium alloy, which subversively killed *Staphylococcus aureus* (*S. aureus*) and *Escherichia coli* (*E. coli*) although only for early infections [14]. Furthermore, as an innovative non-antibiotic approach, the topological structure of the material surface has also demonstrated its intrinsic bactericidal function resulting from the presence of endogenous contact sensitive components in pathogenic microbes [30,31]. For example, previously reported TiO_2 nanopillars on titanium substrate, nanoprotrusions on black silicon, etc. could induce deformation and penetration of the Gram-positive and Gram-negative bacterial cell envelope in contact-killing mode, driven by the mechanical and structural responses caused by the deformation stress imposed by the nanostructure of the peptidoglycan cell wall and inner membrane of bacterial cells, which can inhibit bacterial cell division, reduce bacterial replication and trigger production of reactive oxygen species and increase abundance of oxidative stress proteins to kill pathogenic bacteria [31–34]. In this aspect, the biomimetic mineralized coatings exhibit a variety of rough surface microstructures, which contains many promising biological values [35]. Besides, it is a feasible way to integrate metal ions such as zinc ion into the mineral layer to obtain some potential biological functions [36,37]. Thus, we hypothesized that integration of these alternative approaches which intrinsically possess antibacterial properties onto implant surfaces, could serve as an efficient anti-infection strategy and overcome the shortcomings associated with antibiotic-eluting implants.

To date, there is no antimicrobial system which can accommodate clinical anti-infectious needs at different stages of orthopedic life cycle [38]. Herein, we demonstrate a multilayered coating system leveraging both contact killing mode and eluting killing mode to combat bacterial infections under a variety of scenario of implantation. In view of the emerging prevalence of non-antibiotic technologies, we hypothesized that a zinc incorporated nano-topographical CaP coating on implant surface would provide a trilogy antibacterial strategy to prevent infection during implant life cycle (Scheme 1). In particular, at the early stage (1st week), the CaP nanotopography provides a bacteriostatic surface, possessing a contact-killing effect. At the middle stage (2nd-12th week), key to this system is that the CaP undergo hydrolytic degradation under physiological conditions, thus enabling the sustained release of zinc ions to provide a durable bactericidal effect. At the late stage of implantation, the bottom sodium titanate reservoir still contains enough antibacterial zinc ions to kill bacteria and eradicate established biofilm by contact killing and release killing mode if there are still residual bacterial within the bone or blood circulation. To replicate various clinical scenarios encountered during PJI, we established multiple rat femur models to emulate osteomyelitis, gonitis, intramedullary nails, and revision surgery to validate the feasibility of our trilogy antimicrobial strategy in clinical settings. We also provide a demonstration of translating this approach to commercially available orthopedic implants such as bone fixers and bone nails, showing the clinical value of this technology. Collectively, these data offer a novel antimicrobial approach for infection treatment at different stages of implantation, which may be applicable to a variety of medical device fields.

2. Materials and methods

2.1. Materials

The titanium alloy (Ti6Al4V) plates (8 × 8 × 2 mm), rods (Ø1.0 × 20.0 mm), locking compression plate (LCP, ~14 cm) and pedicle screw (PS, ~7 cm) and were obtained from Canwell Medical Co., Zhejiang, China. Reagent-grade and inorganic salts were purchased from Aladdin Industrial Co., Shanghai, China. Cell counting kit-8 (CCK-8) kit was bought from Beyotime Biotechnology Co., Jiangsu, China. Trimethylaminomethane (Tris; Bio-Rad) and poly-L-aspartic acid (PAsp) (~5.5 kDa, 30 wt% in water; Taihe Co., China) were used without further purification. Reagent-grade absolute ethanol and hydrochloric acid (HCl) were received from Sinopharm Chemical Co., Shanghai. The ultrapure water (18.2 MΩ cm^{-1}) was used in the experiments.

2.2. Pretreatment of Ti6Al4V substrates

The representative surface pre-treatment and modifications of the alloy samples were schematically illustrated in Fig. S1 (Supporting Information (SI)). Firstly, the alloy samples were polished by the diamond pastes (No. 600–2000) and then washed sequentially with absolute ethanol, acetone, and ultrapure water in the ultrasonic cleaner (300 W, 40 KHz; each for 10 min). Then, the samples were soaked in 6.0 mol l^{-1} NaOH solution for 18 h at 60 °C, and followed by washing with ultrapure water and absolute ethanol, respectively. The strong alkali-treated samples were subsequently denoted as AT-Ti.

2.3. Ion exchange treatment

The four groups of ion exchange solutions were prepared with $Sr(NO_3)_2$ and $ZnCl_2$ in ultrapure water, and the initial Sr^{2+} ion concentration was maintained (5.0 mmol l^{-1}) while the Zn^{2+} ion concentrations were increased respectively from 0, 0.200, 1.00–5.00 mmol l^{-1} in the mixture solutions. The pretreated AT-Ti samples were immersed in the $Sr(NO_3)_2$–$ZnCl_2$ mixture solutions (200 mL; see Table 1) and shaken at 120 cycles/min for 6 h. After that, the Sr^{2+} and Zn^{2+} ions were incorporated into the surface layer of newly formed titanate on AT-Ti via

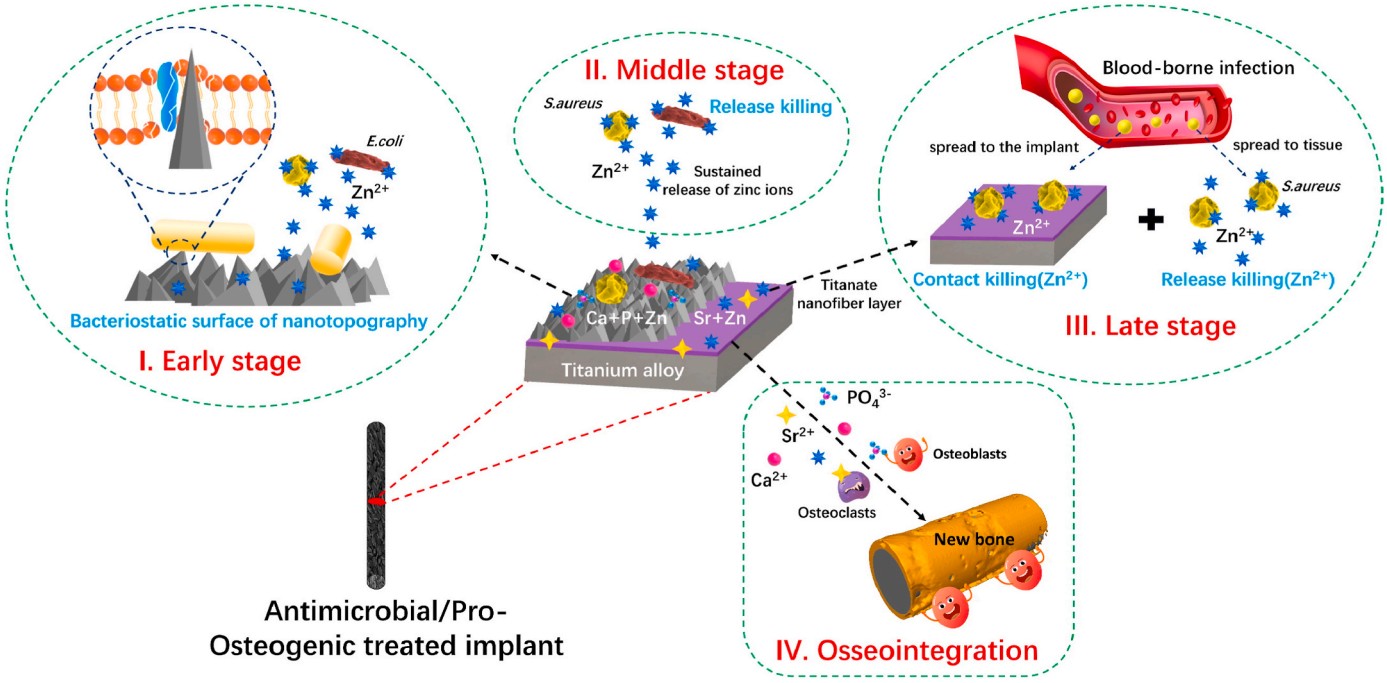

Scheme 1. Schematic illustration of hierarchical structure and composition of the sophisticated Sr–Zn@CaP coating system and the bacterial eradication process (*S. aureus* and *E. coli)* in the form of a trilogy mode at early stage (I), middle stage (II) and late stage (III) *in vitro* and *in vivo* and highly effective osseointegration (IV) triggered by the Ca^{2+}, PO_4^{3-}, Sr^{2+}, and Zn^{2+} in challenging infected scenario.

Table 1
Compositions of working solution used to construct different substrates.

Samples	*Component contents (g) in the solution of ddH_2O* (200 mL)		
	NaOH	$Sr(NO_3)_2$	$ZnCl_2$
AT-Ti	48	–	–
Sr–Zn0	–	0.212	–
Sr–Zn1	–	0.212	0.005
Sr–Zn2	–	0.212	0.027
Sr–Zn3	–	0.212	0.136

ion exchanging with Na^+ ions. Subsequently, the samples were gently washed with ultrapure water and followed by heating to 600 °C at a rate of 3 °C.min^{-1} and maintained this temperature for 60 min, and finally the naturally cooled samples were denoted as AT-Sr-Zn.

2.4. Preparation of CaP coating in modified SBF

The four groups of modified simulated body fluid (mSBF; pH ~7.4) with different inorganic ion compositions (see Table 2) were prepared in ultrapure water and followed by 0.22-μm-pore membrane filtering. The AT-Sr-Zn samples were suspended respectively in the 1000 mL SBF and followed by heating up to 120 °C in a steam-heated autoclave (MLS-3750, SANYO) at a rate of 5 °C.min^{-1}. The solutions suspended with AT-Sr-Zn samples were maintained at 120 °C for 4 h and then naturally cooled. In order to minimize the influence of the natural deposition of precipitates during CaP coating preparation, the mSBF were previously stabilized by adding minor amount of PAsp (1 μM/100 mL mSBF). The CaP-coated AT-Sr-Zn samples were ultrasonically washed with absolute ethanol for three times, and then denoted as Sr-Zn*x*@CaP ($x = 0, 1, 2, 3$).

2.5. Surface characterization of the pretreated samples

Surface morphology, microstructures, and elemental composition were characterized by scanning electron microscopy/energy-dispersive X-ray spectrometry (SEM(3 kv)/EDX(15 kv); Oxford X-Max 80 detector, Zeiss, Germany) and transmission electron microscopy (TEM, 300 kv, FEI Tecnai F30). The surface crystalline phase and chemical composition were determined by X-ray diffraction (XRD; D/MAX 2500 PC, Rigaku, Japan) and X-ray photoelectron spectroscopy (XPS; Thermo Scientific K-Alpha, US). The surface roughness was measured by a 3D atomic force microscopy (AFM) image (NT-MDT Prima; Bruker Dimension Edge; Bruker Dimension ICON).

2.6. Bioactive ion release evaluation

The ion release (Sr^{2+}, Zn^{2+}, Ca^{2+}, PO_4^{3-}) was investigated for the CaP-coated and CaP-eluted (by HCl solution, pH ~3) plate samples ($n = 3$) by incubating in 20 mL Tris buffer (pH ~7.4) at the physiological temperature, to simulate the physiological environment *in vivo*. After soaking at different time intervals (6 h, and 1, 2, 4, 7,15, 21 and 30 days), 1.0 mL of supernatant was centrifuged for inductively-coupled plasma atomic emission spectrometry (ICP-AES, IRIS Advantage ER/S)

Table 2
Compositions of modified SBF used to generate various CaP coatings.

Samples	Component contents (mg) in the mixture solution of ddH_2O (1000 mL)								
	NaCl	$NaHCO_3$	KCl	$K_2HPO_4{\cdot}3H_2O$	$MgCl_2{\cdot}6H_2O$	$CaCl_2$	Na_2SO_4	Tris	$ZnCl_2$
Sr–Zn0@CaP	8035	335	225	277.20	311	350.40	72	6118	–
Sr–Zn1@CaP	8035	335	225	277.20	311	350.40	72	6118	1.363
Sr–Zn2@CaP	8035	335	225	277.20	311	350.40	72	6118	1.363
Sr–Zn3@CaP	8035	335	225	277.20	311	350.40	72	6118	1.363

analysis, and aliquot amount of fresh buffer (1.0 mL) was added into the buffers to maintain the medium volume constant. The inorganic ion cumulative release concentration curve was determined by three parallel samples.

2.7. Antibacterial tests in vitro

2.7.1. Bacterial culture and morphology

Gram-negative *Escherichia coli* (*E. coli*, ATCC 8099) and Gram-positive *Staphylococcus aureus* (*S. aureus*, ATCC 25923) were utilized to evaluate the antibacterial capacity of the alloy samples before and after surface treatments. Luria-Bertani (LB) medium were used to culture the bacterial. A standard procedure was used to prepare sterile LB broth and LB agar plates. The antibacterial capacity of the surface of the alloy plates was determined by the three parallel samples in each group.

To investigate the antibacterial effect of the ion-extracting solution, 100 μL *S. aureus* were cultivated in 5 mL ion-extracting Tris buffer for 24 h and subsequently be inoculated on agar to observe the colonies. To investigate the bacterial morphology and number on the substrate, the *S. aureus* or *E. coli* (100 μL) were seeded on the samples in 24-well culture plate at an initial density of 1×10^6 CFU ml^{-1}. After incubating at 37 °C for 1,3,6,12 and 18 h respectively, the alloy plates were fixed by 2.5% glutaraldehyde at 4 °C overnight, dehydrated sequentially by gradient ethanol (40, 60, 80, 90, 95, 98, and 100% v/v) gradually, and dried with a critical point drier. Finally, the samples were coated by gold before SEM observation [39].

2.7.2. Antibacterial rates

The bacteria were incubated on different plate samples ($n = 5$) at 37 °C for 12 h with *E. coli* and *S. aureus*, respectively. Afterwards, the plates were rinsed by 2.0 mL sterile PBS by ultrasonic vibration for three times. After being serially diluted 10^6 folds, 100 μL of the bacterial solutions were inoculated onto LB plates to culture for 24 h at 37 °C. The picture of the LB plates was visualized by ordinary camera and the number of the colonies was calculated after incubation. The antibacterial rate was carried out by the following equation:

$$\text{Antibacterial rate } (\%) = (A\text{-}B)/A \times 100\%$$

where *A* and *B* represent the CFU counts of control group and experimental group, respectively.

2.7.3. Live-dead fluorescence assay

The antibacterial activity of various samples was measured by live-dead fluorescence assay. Inoculum (1×10^7 CFU/mL) was incubated on prepared samples for 24 h at 37 °C in 24 well plates. Next, the samples were stained by LIVE/DEAD® Baclight™ bacterial viability kit (L7012, Molecular Probes) to investigate bacterial viability. The substrates were washed with 0.9 w/v% saline water and stained using 50 μL of the dye mixture (1.5 μL of SYTO and 1.5 μL of propidium iodide/1 mL of NaCl buffer (0.9%)) for 15 min. Then, the dyed surfaces were analyzed using multi-photon Leica microscope. Five random images from triplicate experiments were obtained for each sample.

2.8. Antibacterial and osteogenesis tests in vivo

2.8.1. Implant-related infection rat models

The osteomyelitis rat model was used to investigate the anti-infection efficacy and biosafty behavior of the modified Ti6Al4V alloy. Approved by the Zhejiang University Ethics Committee of experimental animals, Wistar rats (male, ~4 weeks; ~200 ± 5 g) were randomly divided into three groups in the experiment. After general anesthesia by intravenous injection of 1.5% pentobarbital sodium at a dosage of 4.0 mL kg^{-1}, a 1-cm longitudinal skin incision was made on the bilateral mid-shaft and condyle of femurs in each animal. In the acute osteomyelitis and invert intramedullary nail models, the articular knee cavity was exposed and a channel was drilled by a customized hand-held drill (1 mm) with a low rotary speed and saline irrigation. Subsequently, 10 μL of *S. aureus* (1×10^6 CFU ml^{-1}) was injected into channel by 25-μL microsyringe (Hamilton) before inserting cylindrical rods (Ø 1 × 20 mm).The incision was closed carefully with 5–0 polyglycolic acid sutures (Vicryl) and the rats were allowed to move freely in the cages with enough water and food [14]. In gonitis model, approximately 0.5 mm of titanium rod was left protruding into joint cavity from distal femur, onto which was directly injected 10 μL of the selected inocula of *S. aureus* [40]. In the classic one-stage revision models, the rats went through the first injection of *E. coli* and implantation, followed by a revision at 4 weeks and second injection of *S. aureus* at 16 weeks, and the other operations are the same as described above.

2.8.2. Antibacterial assessment with infection model

To evaluate the antibacterial property of the different surface-modified alloy samples, the infected rats were sacrificed respectively at the 3, 7 days in acute osteomyelitis model, 3 days after bacteria injection in gonitis model, 4 days in the invert intramedullary nail model and 20 weeks in revision models. In acute osteomyelitis models, the pushed rods from the femurs were placed on the sterile agar plates for 5 s and then incubated for 24 h before recording by digital camera. Meanwhile, the femurs were cut in the middle section and implants and femurs were transferred to sterilized centrifugal tubes with 5.0 mL PBS, respectively. Then, the tubes were agitated to detach the bacterial from the femurs and implants. Subsequently, bacterial suspension (100 μL) was dropped on the LB agar plates. After culturing for 24 h at 37 °C, the bacterial colonies were photographed and counted according to the National Standard of China GB/T4789.2 protocol. In the gonitis models, the PBS eluent of the knee joint was performed by a spread plate assay to quantitatively determine the residual *S. aureus*. In the other models, anteroposterior radiographs of the distal femurs were acquired by Faxitron MX-20 (Faxitron Bioptics) and the extracted implants with *E. coli* or *S. aureus* were sequentially fixed, dehydrated and observed under SEM.

2.8.3. Micro-CT scanning and morphology of implant-related femurs

At 4, 8 and 12 weeks after surgery, three rats from each group were sacrificed, and then the femurs were harvested and fixed as mentioned above. The fixed femurs with the implants were subjected to micro-computed tomography (μCT; Skyscan 1172, Bruker Micro-CT, Germany) to evaluate the formation of the bone tissues. The two- and three-dimensional (2D, 3D) images were rebuilt and the surrounding area of rod implants within 0.6 mm was calculated. Data of new bone volume ratio (bone volume/total volume, BV/TV), trabecular thickness (Tb.Th), trabecular number (Tb.N), and trabecular spacing (Tb.Sp) were obtained by supporting software (IAW, Siemens, Germany).The new bone penetration and formed area in the horizontal and coronal scans were quantified by Image J software.

2.8.4. Microbiological and histological evaluation

For inflammatory and osteogenic investigation, following 48 h of immersion in 10% formalin buffer solution, the remaining infected femurs were decalcified using ethylene diamine tetraacetic acid (EDTA) disodium solution (12% *v/v*) for 28 days. Another set of fixed femur specimens was then dehydrated with a gradient of ethanol solution, cleared with xylene, and embedded in polymethylmethacrylate (PMMA). Thereafter, the histological sections perpendicular to the implants (approximately 5 μm for soft-cut and 50 μm for hard-cut specimens) were performed by the Leica SP1600 saw microtome (Leica, Hamburg, Germany). Hematoxylin and eosin (H&E), Gram staining (only for decalcified specimens) and McNeal staining (only for hard-cut specimens) were carried out to observe the infiltration of inflammatory cells (monocytes and neutrophils) and investigate the osteogenic status. Histomorphometric parameters of different sections were also measured with a Leica microscope.

2.9. Mechanical test

The bonding strength of the mineralized coatings was obtained according to ASTM-C633 standard. The coating surface of specimen was boned to metal stripe by epoxy adhesive. Two stubs were aligned and the bonding strength was measured with a crosshead speed of 1 mm min^{-1}. Pull-out test was carried out for each sample at 4, 8, 12 and 24 weeks to evaluate the pull-out strength between the new bone tissues and the rod implant (see Figs. S10A and SI). The notch of the implant was connected to a load cell and then loaded at a constant pulling speed of 0.1 N s^{-1}. The direction of the pulling force is parallel to the long axis of the implant and the extraction force is the maximum load obtained before the implant separated. The bending test of locking compression plates (LCPs), fracture test, macroscopic pull-out test and screwing-in and screwing-out test of pedicle screws (PSs) were measured as shown in the Fig. S10D–F, respectively.

2.10. Statistical analysis

All of the data were reported as means ± standard deviation (SD) and performed in triplicate. The statistical analysis was performed by an OriginPro statistical software package. The statistical differences among groups were measured via the Students's t-test and oneway analysis of variance (ANOVA). $p < 0.05$ was considered statistically significant.

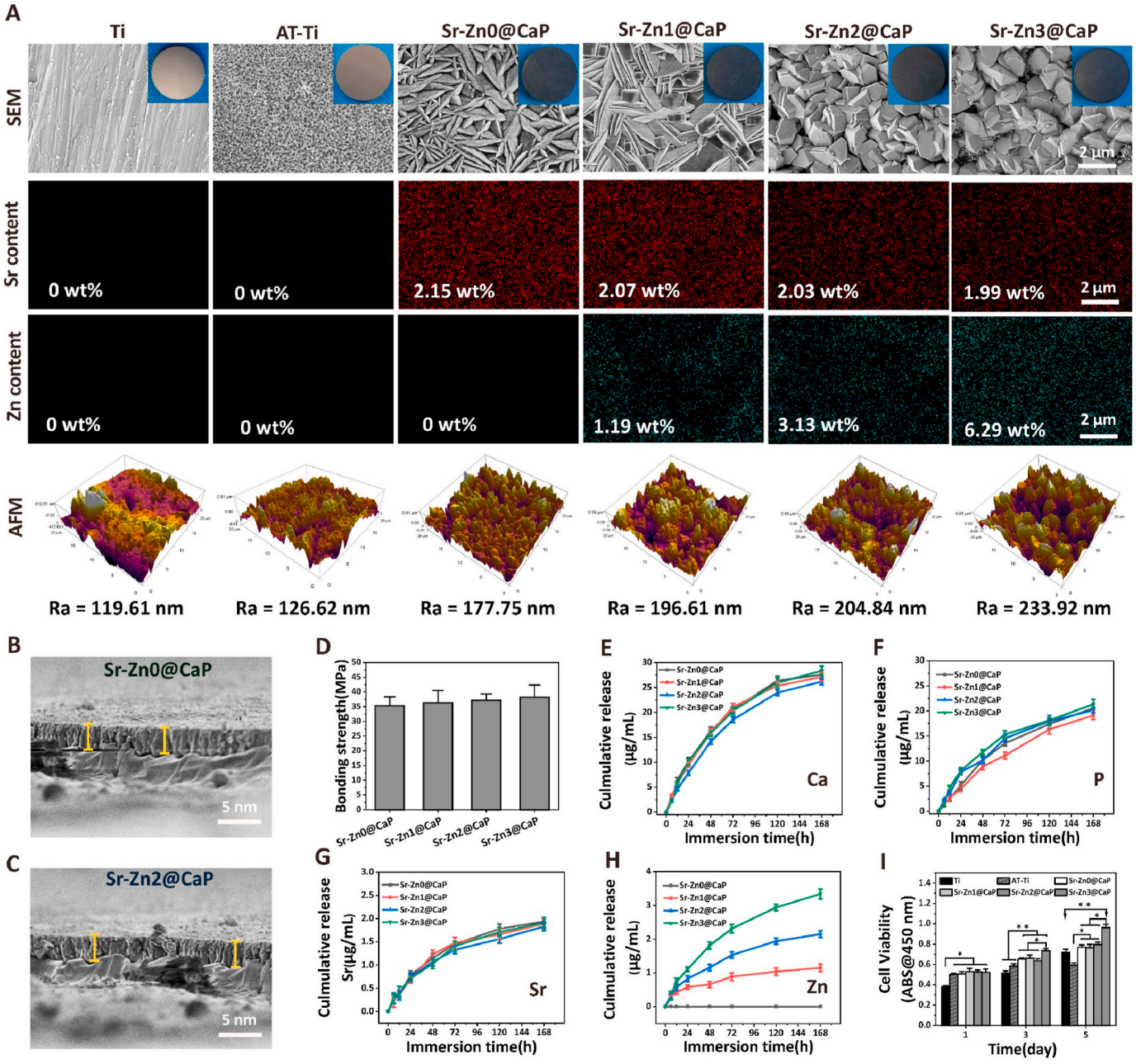

Fig. 1. Designing multifunctional hierarchical coatings for a trilogy of antibacterial treatments and bone regeneration. A) SEM observation, EDX mappings (Sr & Zn) and AFM images of the titanium alloy samples before and after surface treatments, indicating a clear rough coating formation like flake or diamond on the spongy nanoscale network of AT-Ti; B–C) SEM images of cross-sections for Sr–Zn0@CaP and Sr–Zn2@CaP coatings, respectively. D) Bonding strength between CaP coatings and substitute were about 35 MPa under various forming conditions; E-H) Cumulative ion release profiles of Ca^{2+}, PO_4^{3-}, Sr^{2+}, and Zn^{2+} from the different samples in Tris buffer (pH 7.4) within 168 h; I) CCK8 test of BMSCs on the alloy samples before and after surface treatments, showing no detectable cytotoxicity for the Sr-Zn*x*@CaP coatings.

3. Results and discussion

3.1. Systematical characterization of multifunctional coating system

The multifunctional coating system with underlying ion doped titanate layer and upper CaP layer was developed on implant surface via ion exchange, thermal treatment (~600 °C), and followed by biomimetic mineralization in polypeptide-added mSBF via a low-temperature hydrothermal process at ~120 °C. The strontium and zinc were incorporated in sodium titanate porous structures with content level at 1.63 *wt*%, 2.49 *wt*%, respectively, which was achieved by partially replacing sodium (from 5.18 *wt*% to 2.01 *wt*%) in the porous network structures of sodium titanate (Figs. S1 and SI). As shown in Fig. 1A, a spongy nanoscale network was s generated after alkaline treatment, which lay down the foundation for Sr/Zn incorporation. As the thermal and biomineralization progressed, we found a clear, rough, flake or diamond like coating formation from Sr–Zn0@CaP to Sr–Zn3@CaP. EDS mapping demonstrated that strontium and zinc were evenly distributed on the surface, and the strontium content maintained around 2 wt% level while the zinc content was increased gradually (0 *wt*%−6.29 *wt*%) with increase of its concentration in the ion exchange medium and mSBF. According to the AFM results, the surface roughness of various Sr-Zn*x*@CaP (x = 0, 1, 2, 3) groups was 177.75, 196.61, 204.84 and 233.92 nm respectively, which were significantly higher than Ti and AT-Ti groups. The thickness of the coatings were about 3 μm (Fig. 1B and C) and XRD spectra of the coating revealed peaks corresponding to hydroxyapatite (HA, $Ca_{10}(PO_4)_6{\cdot}(OH)_2$) and whitlockite (WL, $Ca_{18}Mg_2H_2(PO_4)_{14}$) (see Figs. S2A and SI), indicating the presence of crystalline biphasic composites. HA phase and WL phase accounts for about 81.20 *wt*% and 18.80 *wt*% in Sr–Zn0@CaP group while about 93.00 *wt*% and 7.00 *wt*% in the other three groups, respectively. Besides, TEM images revealed that the CaP coatings, for example Sr–Zn0@CaP and Sr–Zn2@CaP, were mostly consist of nanostructured flake-like or granule-like phases, consistent with SEM observation (see Figs. S2B, C, SI). Moreover, XPS spectrum demonstrated the major peaks for Ca 2p, P 2p, O 1s and C 1s, indicating that CaP coatings were already formed on the surface of titanium (Figs. S2D and SI). The peaks of C 1s and N 1s were mainly attributed to carbonate and PAsp in the mineralized solution, respectively. In addition, the high-resolution spectra could also identify the peaks of Zn 2p and Sr 3 d but no obvious peaks of Ti 2p and Al 2p in the layer, implying that strontium and zinc metal elements were limitedly integrated in the CaP coating (Fig. S2E−H, SI). The presence of strontium might be due to the re-organization of the underlying titanate structure during mineralization while the zinc elements may be originated from the titanate structure and the zinc ion in the mSBF solution.

For underlying layer, ion exchange was occurred on the NaOH-etched surface of Ti6Al4V where Na^+ ions in the sodium titanate porous structure were replaced by Sr^{2+} and Zn^{2+} ions and sequential heat treatment stabilized the loaded ions with sustained release properties [41,42]. This Sr^{2+}/Zn^{2+}-containing sodium titanate porous layer was chosen as a reservoir of metal ions due to its capability to gradual release Sr^{2+}/Zn^{2+} ions and the CaP was chosen as a controller of ion release due to its slow degradability. Moreover, the binding strengths about 35 MPa of the various coatings were obtained under various forming conditions (Fig. 1D), which is substantially higher than well accepted industrial standard set at 25 MPa according to ISO 9693 [43]. This data implies that increased temperature might not only accelerate the biomimetic mineralization reaction but also improve the integration of the fibrous coating with the substrate and resulted in higher interfacial strength. Besides, CCK-8 cell viability test showed that incorporation of Sr/Zn together with CaP did not cause detectable cytotoxicity, indicating the introduction of antimicrobial ions does not sacrifice the biocompatibility of the implants (Fig. 1I). Synthetically, the upper and underlying layers were combined together to form a sophisticated hierarchical system which allow them to exert their corresponding biological functions on the implants.

Sustained ion release from coating system is of critical importance for the success of our strategy as it provides sufficient potency to fight bacterial infection on implants [14]. As shown in Fig. 1(E−G), calcium, phosphate and strontium exhibited similar gradual release patterns over a time period of 168 h regardless of varying Zn amount incorporated into the coatings. In contrast, we observed cumulative release of Zn increased as the amount of Zn incorporated in the coatings increased. The Sr–Zn3@CaP and Sr–Zn0@CaP samples showed the highest and lowest zinc concentration at each time point (Fig. 1H), implying the zinc release kinetics was directly related with its content in the ion exchanging layer. Interestingly, there were no significant difference in degradation behaviors of calcium and phosphate in coating system with increasing Zn contents in the ion exchanging layer.

3.2. CaP nanotopography generate a bacteriostatic surface at early stage

The first 4–6 h upon implantation represents the critical period for antibacterial effect of implants [44], thus the antibacterial activity of the as-prepared coatings was evaluated against gram-positive *S. aureus* and gram-negative *E. coli* at 6 h (Fig. 2A; Figs. S3 and SI). Both *S. aureus* and *E. coli* maintained their intrinsic oval- or rod-like morphology on AT-Ti group while they showed abnormal appearance on Sr-Zn*x*@CaP surfaces. Moreover, the amount of the bacteria on Sr-Zn*x*@CaP surface decreased substantially when compared to AT-Ti. Damaged bacteria with envelope deformation or warped membranes (Red arrows) were observed in the Sr-Zn*x*@CaP groups, and many were completely lysed (blue arrows). In order to determine the bacteriostatic rate on the coatings against *S. aureus* and *E. coli*, a quantitative analysis for up to 18 h of bacteria incubation on the coating surfaces were determined by counting colony numbers from bacteria eluate (Fig. 2B and C). AT-Ti samples showed very limited antibacterial activity (below 30%) from 1 to 6 h, whereas CaP-coated samples (i.e. Sr–Zn0@CaP, Sr–Zn2@CaP) showed an antibacterial rate of above 50% against *S. aureus* and *E coli* after 3 h of incubation. As the culture continued to 18 h, these two types of coatings maintained efficient antibacterial capability against *S. aureus* (~70% in Sr–Zn0@CaP, ~90% in Sr–Zn2@CaP) and *E. coli* (>75% in Sr–Zn0@CaP, > 95% in Sr–Zn2@CaP) while AT-Ti only showed antibacterial rate below 30%. Interestingly, the level of strontium ions in our study was not detected to have distinct antibacterial effect through SEM observation of *S. aureus* incubated on the AT-Sr surface and antibacterial experiment based on Sr^{2+}-extracting solutions. Moreover, the release of Sr ions in the coatings is very weak, especially in the middle and late stages mentioned later (Figs. S4 and SI). Thus, the antibacterial effect of Sr–Zn0@CaP group was not caused by the presence of Sr, suggesting that intrinsic property and morphology of CaP coating may contribute to the observed antimicrobial property. Many precious reports have confirmed that the unique topological morphology and corrugated surface structure could damage the microorganism through intrinsic bacteriostatic process [39,45–48]. In addition, increased surface roughness at the microscale significantly inhibit bacterial adhesion and biofilm formation on its surface [48,49]. Moreover, increased surface electrical potential may suppress the bacterial adhesion via electrostatic repulsion at this stage [50–52], which was consistent with precious reports that the negative charge of sample surface was significantly increased by the increasing roughness at the microscale [49]. Collectively, the early-stage bacteriostatic potential of our coating systems (Sr–Zn0@CaP *vs* Sr–Zn2@CaP) may be more dependent on their intrinsic surface microstructure and composition, which is very important to prevent early infection.

The *in vivo* antibacterial effect of the coatings was evaluated using an acute rat osteomyelitis model shown in Fig. 2D. Macroscopically, the control group (AT-Ti) showed a severe infection with abscesses and bacterial membranes (Fig. 2E). Around the implants at 3 and 7 days of post-implantation. In comparison, Sr–Zn0@CaP group exhibited only a slight infection, and there was no detectable infection in the Sr–Zn2@CaP group after 3 days. No infection was observed in the two

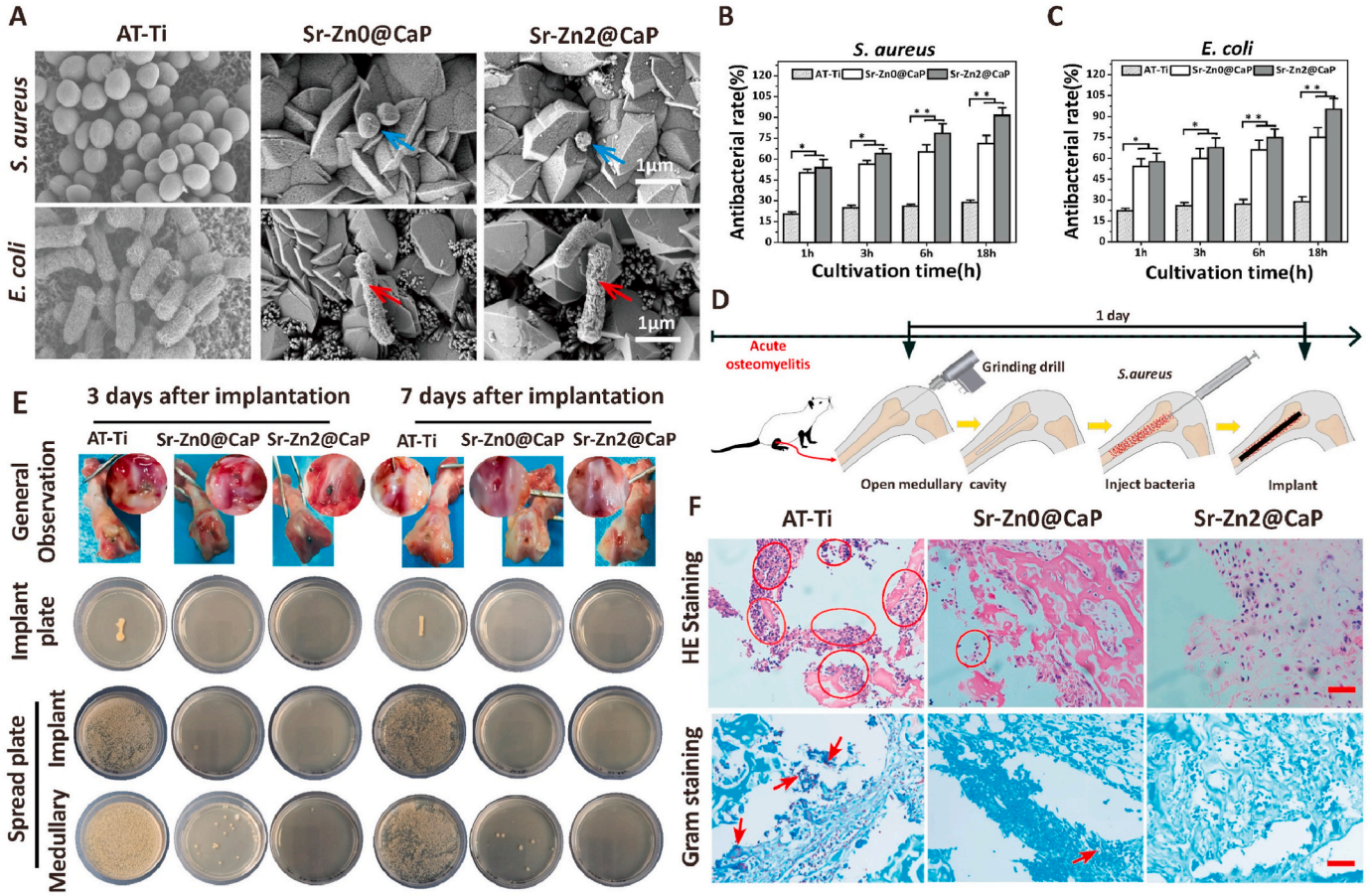

Fig. 2. Early-stage antibacterial efficacy evaluation *in vitro and in vivo*. A) SEM micrographs of *S. aureus* and *E. coli* incubated on different samples for 6 h, the arrows showing deformed bacterial membrane; B–C) Time-dependent antibacterial rates of different sample surfaces (AT-Ti, Sr–Zn0@CaP, Sr–Zn2@CaP) against *S. aureus* and *E. coli*, $n = 4$ pre group, $^{*}p < 0.05$ and $^{**}p < 0.01$; D) Experimental procedure of acute rat osteomyelitis model to test antibacterial efficiency of implants *in vivo*; E) Rat distal femur, implant imprint and spread plate images of different rod surfaces or surrounding medullary cavities after implantation for 3 and 7days with *S. aureus* infection; F) H&E immunohistochemistry and Gram staining images in the regions of femur osteoepiphysis with different implant rods at 3 days post-implantation, respectively (scale bar: 50 μm), red circles representing lymphocytes and neutrophils infiltration and red arrows representing inflammatory cells with bacteria.

experimental groups implanted with Sr–Zn0@CaP and Sr–Zn2@CaP 7 days after surgery. From the images of imprint and agar plate *ex vivo*, a severe bacterial infection was identified in the AT-Ti group at 3 and 7 days post operation. On the contrary, few bacteria colonies were identified in the Sr–Zn0@CaP group and no bacteria was detected in the Sr–Zn2@CaP group at two time points (Fig. 2E, panels). In addition, the quantitative analysis (Fig. S5, SI) further demonstrated that the Sr–Zn0@CaP and Sr–Zn2@CaP groups exhibited an excellent anti-infection capability on the surface of implant against *S. aureus* (~92% at 3 days, more than 96% at 7 days), and especially the later exhibited better anti-infection efficiency in the bone marrow cavity (>80% in 3 days, more than 90% in 7 days) among three groups ($p < 0.05$).

The inflammation reaction and bacteria residues at the infection sites *in vivo* were further evaluated by hematoxylin and eosin (H&E) and Gram staining. As shown in Fig. 2F, large amounts of monocytes and neutrophils (red circles), as well as residue *S. aureus* (red arrows) were observed in AT-Ti group. Few or no inflammatory cells or residue bacteria were detected in the Sr–Zn0@CaP and Sr–Zn2@CaP groups, suggesting the coating system has effectively eliminate the initial bacterial invasion. This observation was also consistent with our quantitative analysis *in vivo*. In orthopedics, the rapid adhesion of bacteria to the biomaterials surface is the most critical step in forming prosthetic infection in the early stage of implantation [53]. In response to early adhesion, we specially formed a generated adhesion-resistant and bacteria-repellent a surface on implants through CaP coating to inhibit bacterial adhesion. As our preliminary study showed that strontium ion could only provide very limited bacteriostatic effect (Fig. S4, SI), we speculate that the surface modification of CaP coating exert remarkable bacteriostatic properties at early stage and zinc ion release enhanced this bacteriostatic performance, which addressed the first risk factor of bacteria adhesion for prosthesis infection after implantation.

3.3. Sustained zinc release from mineral system lead to bactericidal performance at middle stage

Sustained release of antibacterial ions holds the key for the success of our strategy. We have shown Zn^{2+} could be gradually released from the coatings *in vitro*, which may trigger the release-killing mode once the coating starts to degrade *in vivo* (Fig. 3A). The Sr-Zn*x*@CaP systems displayed certain degree of degradation and CaP morphologies became blurred after immersion. EDX analysis also confirmed decrease of strontium and zinc in the coating layer after degradation for 12 weeks (Figs. S6 and SI). Specifically, zinc content dropped from 3.2% to 2.41% after 12 weeks (Fig. 3B). In turn, the local zinc dose maintained between 1.2 and 1.6 μg/mL/day, which was maintained above minimum inhibitory concentration at various time pints (Fig. 3C).

In order to demonstrate sustained antibacterial capability of the coatings *in vitro*, we conducted two set of experiments: in the first set of experiments, both *S. aureus* and *E. coli* were directly seeded on 12-week degraded coatings, only Sr–Zn2@CaP group exhibited substantial

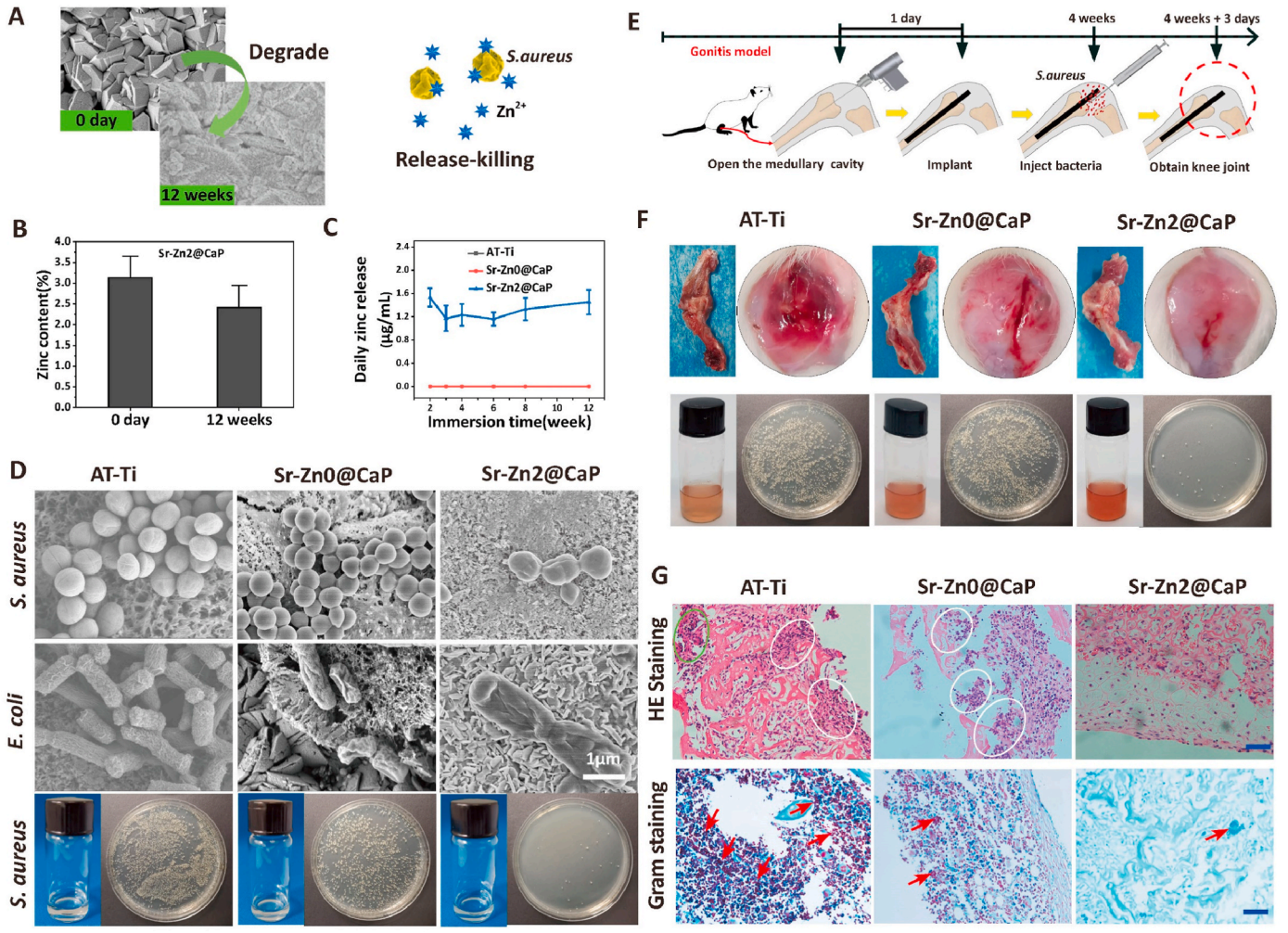

Fig. 3. Intermediate-stage antibacterial efficacy evaluation *in vivo* and *ex vivo*. A) The changes of microstructure and surface morphology of the samples before and after soaking in Tris buffer (pH 7.4) for 12 weeks. The following pattern represent Zn^{2+} release-dependent antibacterial mechanism. B) Statistics of zinc content in Sr–Zn2@CaP sample dropped from 3.2% to 2.41% after soaking in the Tris buffer (pH 7.4) for 12 weeks. C) The daily zinc release of different samples in 2, 3, 4, 6, 8 and 12 weeks. D) SEM images of both *S. aureus* and *E. coli* morphology on the surfaces of various samples after soaking in the Tris buffer for 12 weeks. The last row shows the spread plate images of *S. aureus* seeding in the corresponding extraction solution. E) The primary procedure of rat knee model to mimic gonitis symptom where *S. aureus* were injected into the knee cavity 4 weeks after implantation. F) The macroscopic observation of knee-joint post-implantation and the *ex vivo* colony culture test for the knee joint eluate. G) H&E immunohistochemistry and Gram staining images in the regions of femur osteoepiphysis with different implant rods at 3 days after bacterial injection, respectively (scale bar: 50 μm). Circles represent lymphocytes and neutrophils infiltration. Red arrows represent inflammatory cells with bacteria.

bacteria reduction accompanied with membrane concavities and wizened status of the bacteria after culture; similar results were observed when we added coating extract medium to agar plates and only Sr–Zn2@CaP showed few bacteria colonies on its in Fig. 3D. Collectively, these data clearly demonstrated that our designed coating system enabled zinc ions release long enough which would combat mid-term (up to 12 weeks) bacteria infection. Previous study has proved that Zn^{2+} has an outstanding antibacterial property by generating excess reactive oxygen species (ROS), liberating damaging hydroxyl radicals (·OH) and toxic $O_2^{\cdot-}$ and H_2O_2 [54,55]. Sustained Zn^{2+} released during the natural degradation of the mineral coating produced killing effect by these intracellular mechanisms and it is thus important to fight infection in the middle stage after implantation.

In the second set of experiments, we used rat knee model to mimic gonitis symptom where *S. aureus* were injected into the knee cavity 4 weeks after implantation. As shown in Fig. 3E, the knee-joint specimens obtained from the AT-Ti and Sr–Zn0@CaP groups exhibited severe infection, with abscesses and bacterial mucus. On the contrary, no macroscopic inflammatory reaction was visible in Sr–Zn2@CaP group (Fig. 3F). Also, the *ex vivo* colony culture test for the knee joint eluate exhibit similar trend as the colony number on Sr–Zn2@CaP agar plate was significantly fewer than the other tested groups. H&E and Gram staining further verified above observation (Fig. 3G). Severe neutrophil infiltration and acute inflammation were detected for AT-Ti and Sr–Zn0@CaP groups (white circles). Very few neutrophils and gram-positive cells were found in the Sr–Zn2@CaP group. Taken together, incorporation of zinc in the coating system effectively inhibit bacterial infection both *in vitro* and *in vivo*, even after a significant amount of degradation time. Although many studies have demonstrated certain metal ions possessed potent antibacterial properties in a variety of implants, they have mainly focused on their initial impact on fighting infection, which was mainly executed via burst release of ions. For instance, Hegemann et al. developed Ag-containing plasma polymer coatings which can provided an effective peak release of Ag ions to offer a strong adjacent antibacterial effect [56]. Instead, we have particularly focused on long term antimicrobial effect of zinc ions in our study. Since our coating design allowed gradual release, as well as considerable ion reservation during coating degradation, sustained antibacterial effect

has been achieved in multiple animal models. The high antibacterial level remained in the pseudo-revision model suggests that this system may perform better in term of anti-infection in these prevalent clinical conditions.

3.4. The residual zinc in fibrous titanate induced a strong bactericidal properties at late stage

In order to verify the late stage antibacterial efficacy, all residual coatings after immersion in Tris buffer were removed by acid for bacteria growth test. Fig. 4A shows the morphological restored from CaP coating to the fibrous titanate substrate. Zinc content in the Sr–Zn2@CaP coating was about 1.60 wt% after the CaP coating was dissolved (Fig. 4B). In particular, the residual zinc in titanate substrate was released in a sustained manner with daily release dosage at about~2.5 μg/ml/day as we extended the immersion study (Fig. 4C). Even after one year of implantation in rats, the zinc content in the Sr–Zn2@CaP coating can be still detected about level of 0.82 wt% (Figs. S7 and SI). When *S. aureus* and *E coli* were seeded on the acid-etched surfaces, we found high-density *S. aureus* and *E coli* colonies on AT-Ti and eluted Sr–Zn0@CaP groups (Fig. 4D; Figs. S8 and SI). As for Sr–Zn1-3@CaP group, it was found that not only the bacterial density remarkably decreased, but also much bacteria death was observed with a remarkable damage on their appearance and a clear envelope deformation (marked by orange and yellow arrows). The live and dead staining of bacteria was also consistent with the above results (Figs. S9 and SI).

Subsequently, we conducted two set of animal studies to validate the long-term antibacterial and *anti*-biofilm efficacy. In the first study, acid-etched implant was inserted into medullary cavity after *S. aureus* injection and it was pulled out after 3 days (Fig. 4E). SEM examination of the explants showed that a large number of *S. aureus* were found on the surface of AT-Ti and Sr–Zn0@CaP rod. In contrast, no bacteria were identified on the Sr–Zn2@CaP rod. This test confirmed that the residue zinc on the implants after acid-etching could still play a pivotal role during bacterial infection and effectively eliminate bacteria *in vivo*.

In the second study, we designed a rat model to specifically mimic implant revision in clinical setting. An osteomyelitis model was firstly created and the rod was implanted. A second bacteria injection was given to replicate the possible infection during implant revision (Fig. 4F). To explore the response of the distal femur to *S. aureus* infection, distal femoral width was precisely measured via X-ray. The

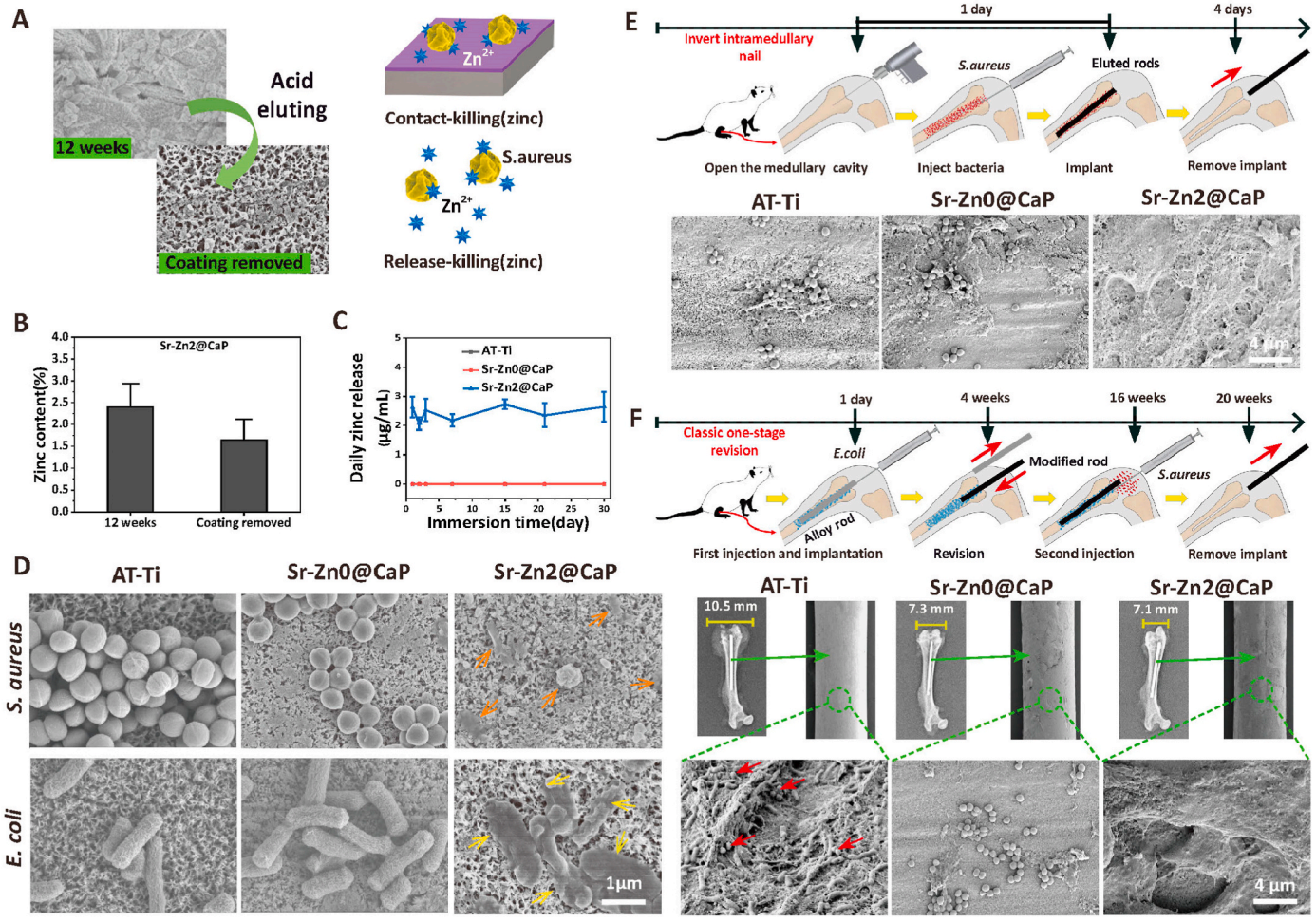

Fig. 4. Late-stage antibacterial efficacy evaluation *in vitro* and *in vivo*. A) The morphological restored from CaP coating to the fibrous titanate substrate of the Sr–Zn2@CaP samples after acid eluting by HCl solution (pH = 3). The following pattern represent expected contact-dependent and release-dependent antibacterial mechanism of residual zinc. B) Statistics of zinc content in Sr–Zn2@CaP sample after the CaP was eluted by the HCl solution (pH ~3). C) The daily zinc release of the CaP-eluted samples on 1, 2, 3, 7, 15, 21 and 30 days. D) SEM images of both *S. aureus* and *E. coli* morphology on the surfaces of various CaP-eluted samples. Black arrows represent dissolved and shriveled *S. aureus*. Red arrows represent ruptured and dissolved *E. coli*. E) The operation procedures of inverted intramedullary nail in rat models and SEM images of *S. aureus* on AT-Ti, Sr–Zn0@CaP eluted and Sr–Zn2@CaP eluted rods taken from rat femurs, $n = 5$ per group. F) The osteomyelitis modeling of *E. coli*, revision surgery, second injection of *S. aureus* in rat models. Representative X-ray images: yellow bars indicate distal femoral width. The SEM images of biofilm of *S. aureus* and *E. coli* on AT-Ti, Sr–Zn0@CaP and Sr–Zn2@CaP rods taken from rat femurs after first *E. coli* injection, one stage revision and second *S. aureus* injection. Red arrows represent mixed *S. aureus* in the biofilm of *E. coli*, $n = 5$ per group.

average width of rat distal femoral bone in AT-Ti group revealed 10.5 ± 0.3 mm, which was significantly greater compared with those in the Sr–Zn0@CaP (7.3 ± 0.2 mm) and Sr–Zn2@CaP (7.1 ± 0.2 mm) ($p < 0.05$). Importantly, AT-Ti implant showed a large-area confluent layer of concomitant mature biofilm of *E. coli* and *S. aureus*, while only a small number of *S. aureus* were found on the Sr–Zn0@CaP rod; however, Sr–Zn2@CaP group showed no detectable *E. coli* or *S. aureus* either at 16 weeks or after revision under SEM.

According to our investigation, *S. aureus* and *E coli* showed potent backup bactericidal properties in the Sr-Zn*x*@CaP-eluted groups (x = 1–3) *in vitro* and *vivo*, especially the notably strong antibacterial effect can be still measured in the Sr–Zn2@CaP group through 20 weeks *in vivo*. Definitely, the delayed and late infections in orthopedics often occur after several months or even several years after surgery which are very difficult to intervene due to the their hidden onset and antibiotic resistance [57,58]. As for these issues, the underlying layer containing zinc is specially customized to serves as an antibacterial reserve to deal with infections that may occur any time after implantation [59]. Therefore, this hierarchical coating system not only possess excellent antibacterial effect at the early stage post operation, but also has a critical role in fighting against possible infections throughout its whole life cycle.

3.5. Bone regeneration evaluation associating with the infection of implant

Superior osseointegration stands for the overarching requirement towards clinically successful orthopedic implants [60]. This feature is of particular significance at the initial stage of implantation associated with infection as such vulnerable environment could easily break the balance between antibacterial effect and osseointegration of our designated system [61], thus new bone formation surrounding the implants with infection was evaluated using an intramedullary model (Fig. 5A). Micro-CT analysis revealed distinct osseointegration progress between three tested groups: AT-Ti showed poor new bone coverage throughout the entire implantation period with scattered new bone around the rod; Sr–Zn0@CaP group was covered by more new bone at 4 weeks and this trend continued in the next 8 weeks. However, its bone distribution around the implant appeared to be heterogeneous. Sr–Zn2@CaP exhibited more new bone coverage at all three time points compared to

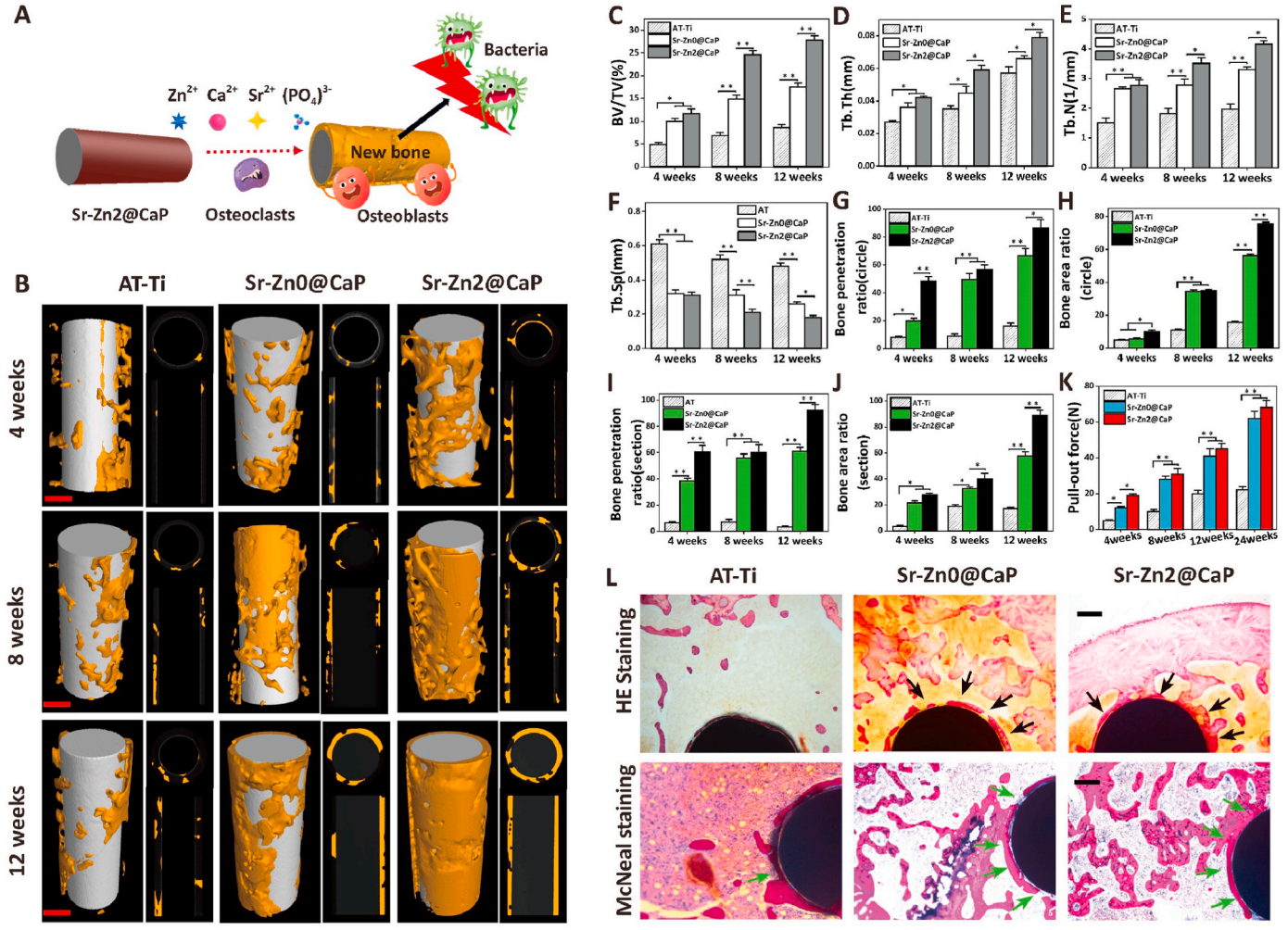

Fig. 5. High-efficiency osseointegration evaluation *in vivo*. A) New bone formation surrounding the implants with infections and proposed osseointegration mechanism in an intramedullary model. B) Representative 3D reconstruction of new bone around implants, 2D transaxial images and 2D coronal image of new bone penetration and new bone area in the regions of osteoepiphysis in infected intramedullary models at 4, 8, and 12 weeks after surgery (scale bars = 0.5 mm). Quantitative statistics of C) BV/TV, D) Tb.Th, E) Tb.N, F) Tb.Sp in 3D reconstruction by micro-CT. Quantitative analysis of G) new bone penetration rate and H) new bone area rate around implants from the histomorphometric measurements in the horizontal plane. Quantitative analysis of I) new bone penetration rate and J) new bone area rate around implants from the histomorphometric measurements in the coronal plane. K) Quantitative statistics of pull-out force at predetermined time points. K) Histological images of bone sections around the implants by H&E and McNeal staining. Black arrows and green arrows both indicate the new bone formation around implants (scale bars = 200 μm). n = 4 per group, *p < 0.05 and **p < 0.01.

other two groups. Moreover, new bone distributed more evenly throughout the length of the implants (Fig. 5B). Quantitative analysis involving BV/TV, Tb.Th, Tb.N, and Tb. Sp revealed consistent results as for qualitative observation (Fig. 5C–F). Moreover, the Sr–Zn2@CaP showed the highest new bone penetration and most new bone formation area (Fig. 5G and H) in the horizontal and coronal scans of μCT (Fig. 5I and J), while these measurements in AT-Ti and Sr–Zn0@CaP groups were significantly lower.

Interfacial strength represent the gold standard for implant integration [62]. Pull-out tests at various time points revealed that the pull-out force of all tested groups increased as implantation time extended (Fig. 5K). Although the pull-out strength remained low at 4 weeks, Sr–Zn0@CaP and Sr–Zn2@CaP groups showed higher value compared to AT-Ti group. This trend continued and coated implants demonstrated higher pull-out strength at all the time points. At 24 weeks, the pull-out strength of Sr–Zn2@CaP was around 65 ± 8 N, which is three times of AT-Ti group. SEM images of implants after testing presented limited bone tissue on the surface of rods in AT-Ti group, while large portions of bony tissue and periosteum were integrated inside CaP coating cracks of rod implants in Sr–Zn0@CaP and Sr–Zn2@CaP groups (Figs. S7A and SI). The excellent mechanical pull-out properties between the bone and implants of Sr–Zn2@CaP were attributed to (i) normal bone integration with no signs of infection in a microenvironment rich in zinc ions, and (ii) complete bone coverage and penetration around the implants, confirming that the calcium, phosphorus, and strontium release from strontium integrated CaP coating system are highly effective at promoting osseointegration of interface, especially in this challenging infected scenario with bacteria-induced trauma to host bone and surrounding soft tissue.

H&E and McNeal straining (Fig. 5L) were consistent with μCT observation. As for the AT-Ti group, plenty of fibrous tissues were dominantly filled and no obvious hint of new bone was observed. In Sr–Zn0@CaP group, large amount of new bone tissue was found at the interface between the implant and the bone (black and green arrows), but there were still some bone discontinuities due to insufficient antibacterial performance without bactericide. In contrast, the bone network had remarkable continuity with cancellous bone in Sr–Zn2@CaP group, and there was full coverage of newly formed bone tissues detected from host-implant interface (black and green arrows), implying incorporation of zinc in the coating could remarkably promote osseointegration under infectious condition.

Prompt integration of implants into host tissue is crucial for the success of prosthesis implantation in orthopedics [63]. Distinct osseointegration levels were obtained from implants with various coating systems (Fig. 5). We reasoned that the interplay between antimicrobial activity and osteogenic potency of the implants may be the key factors determining osseointegration level under infectious environment. Poor integration of AT-Ti group may be caused by lack of both antimicrobial and osteogenic properties, which led to limited peri-implant bone formation, heavy fibrous invasion, and low bonding force. On the other hand, Sr–Zn2@CaP group provided excellent antimicrobial property via CaP nanotopography and zinc ion release, so that bacteria at the implantation sites could be quickly eliminated, providing an environment conducive for bone formation. Meanwhile, incorporation of strontium may contribute to osseointegration via its proven capability has been proven to of triggering new bone formation through enhanced osteoblastic activity [64,65]. In the context of infectious bone implantation, the synergy between antibacterial and osteogenic properties ought to be the two unreplaceable determinants leading to rapid and strong osseointegration [36].

3.6. Clinical translation prospect and design philosophy

Prosthetic infections are often disastrous complication needed initial debridement and re-implantation, thus novel prosthesis with excellent antimicrobial property are urgently needed in clinic [66,67]. We have successfully translated our coating technology into clinically standard orthopedic implants such as locking compression plate (LCP) and pedicle screw (PS) (Fig. 6). Our multifunctional coating system was converted from samples about 1 cm scale to large irregular orthopedic prosthesis with standard size (Fig. 6A). The LCP and PS exhibited the similar coating surface morphology, uniform distribution of calcium, phosphorus, strontium and zinc after treatment (Fig. 6B and C). More importantly, the modified prosthesis surface exhibit strong bactericidal rate of about 85% to *S. aureus* and *E. coli*, while control prosthesis does not show antibacterial properties (Fig. 6D–F). PS shows improved torsional strength in the screw-in and screw-out and the pull-out tests on the simulated human bone, which may be attributed to the rough nano-topography surface (Fig. 6G and H). Moreover, the macroscopic mechanical testing reveal that the modified implants retain the same bending and fracture strength, indicating the modification treatment did not sacrifice the original mechanical properties and structural stability of the implants (Figs. S10G, H, SI). Collectively, we have clearly demonstrated that the trilogy strategy developed in this study could be readily translated onto standard orthopedic medical devices, which further validates the clinical significance of our technology in treating implant-associated infection in orthopedic and other fields.

4. Conclusions

In summary, a hierarchical coating system was successfully fabricated through hydrothermal reaction and biomimetic mineralization. This sophisticated system has been proven to have excellent antibacterial effects against *S. aureus and E. coli* both in *vitro* and *in vivo*. The nanotopography in the top layer can mediate bacteriostatic activity derived from intrinsic antibacterial property from CaP at the early stage of infection. With the slow biodegradation of the CaP coating, the sustained release of Zn^{2+} can contribute on inhibiting bacteria activity and biofilm formation for several months above the MIC in “release-killing” mode at the intermediate stage. Once CaP coating is degraded completely, the underlying zinc titanate layer is exposed for long-term antibacterial activity in “contact killing” and “release killing” mode simultaneously at the late stage. Additionally, the results *in vivo* experiments demonstrated that the established bacterial biofilm on Sr–Zn2@CaP implant could be effectively eradicated after 20 weeks. Moreover, sustained release of Sr^{2+} and Zn^{2+} during CaP coating degradation substantially promoted implant osseointegration even under an infectious environment by showing more peri-implant new bone formation and substantially improved bone-implant bonding strength. Besides, we confirmed that calcium phosphate coating containing strontium and zinc can greatly promoted interfacial bone integration and achieved tight bonded strength between bone and metal surface in the challenging osteomyelitis scenario. Therefore, this facile, versatile and effective trilogy antimicrobial strategy has the potential to be used in a wide range of biomaterials and implant applications, to directly benefit patients who rely on the rapid growth of prosthetic implants.

CRediT authorship contribution statement

Yikai Wang: Conceptualization, Writing - original draft, Writing - review & editing, Methodology, Investigation, Software, Data curation, Formal analysis, Validation. **Wangsiyuan Teng:** Methodology. **Zengjie Zhang:** Methodology. **Xingzhi Zhou:** Visualization. **Yuxiao Ye:** Writing - review & editing. **Peng Lin:** Visualization. **An Liu:** Visualization. **Yan Wu:** Visualization. **Binghao Li:** Visualization. **Chongda Zhang:** Writing - review & editing. **Xianyan Yang:** Visualization. **Weixu Li:** Visualization. **Xiaohua Yu:** Conceptualization, Writing - review & editing, Supervision, Visualization. **Zhongru Gou:** Conceptualization, Resources, Writing - review & editing, Supervision. **Zhaoming Ye:** Conceptualization, Writing - review & editing, Resources, Project administration, Supervision, Funding acquisition.

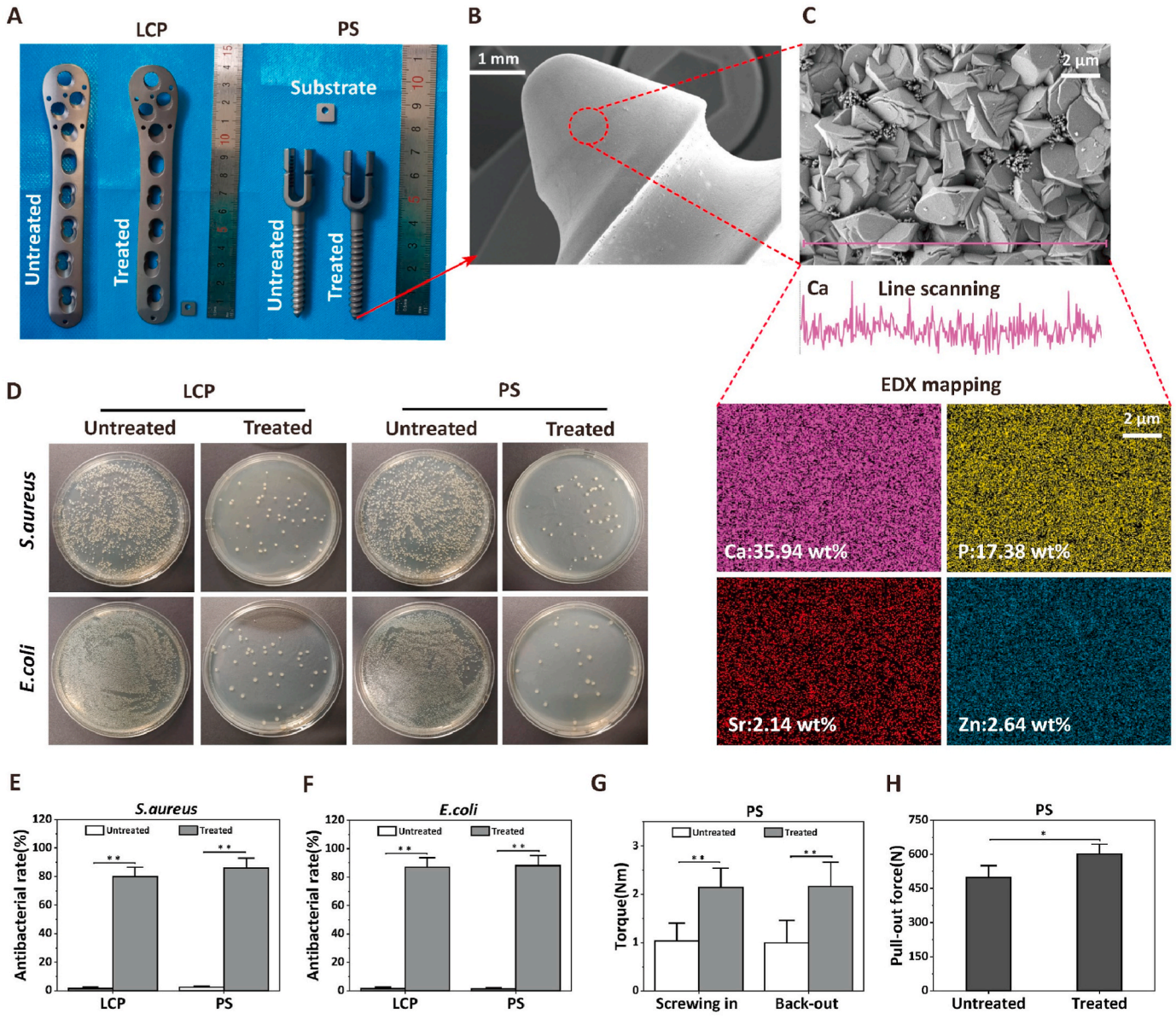

Fig. 6. Surface engineering titanium alloy devices with the new multifunctional coating strategy potentially favorable for the next-generation clinical application. A) General observation of locking compression plate (LCP) and pedicle screw (PS) before and after the coating treatment. B–C) Representative low- (scale bars = 1 mm) and high-magnification (scale bars = 2 μm) SEM images of screw tip of PSs, including line scanning of Ca element and EDX mapping of Ca, P, Sr and Zn elements. D) Spread plate images of *S. aureus* and *E. coli* seeding on the surface of corresponding plates and screws before and after the modification of the novel approach. Quantitative statistics of antibacterial rate on the surface of LCPs and PSs against E) *S. aureus* and F) *E. coli* after culturing for 12 h. H) Actuating properties test of pedicle screw. The Sr–Zn2@CaP coated PSs showed statistically higher screwing in and back out torque compared to untreated PSs. F) Pull-out test in PSs. The Sr–Zn2@CaP coated PSs showed statistically higher pull-out force compared to untreated PSs, $n = 6$ per group, $^{*}p < 0.05$ and $^{**}p < 0.01$.

Declaration of competing interest

The authors declare that they have no known competing financial interests or personal relationships that could have appeared to influence the work reported in this paper.

Acknowledgements

Y.W., W.T., and Z.Z. contributed equally to this work. This work was financially supported by the National Key Research and Development Program of China (Grant No. 2018YFC1105401, 2018YFC1105404), National Natural Science Foundation of China (81702118,31870959), 2018 Zhejiang University Academic Award for Outstanding Doctoral Candidates and Medical and Health Science and Technology Plan of Department of Health of Zhejiang Province (WKJ-ZJ-1821).

Appendix A. Supplementary data

Supplementary data to this article can be found online at https://doi.org/10.1016/j.bioactmat.2020.11.030.

References

[1] B. Kapadia, R. Berg, J. Daley, J. Fritz, A. Bhave, M. Mont, Periprosthetic joint infection, Lancet (London, England) 387 (10016) (2016) 386–394, https://doi.org/10.1016/s0140-6736(14)61798-0.

[2] T. Peel, K. Buising, P. Choong, Prosthetic joint infection: challenges of diagnosis and treatment, ANZ J. Surg. 81 (2011) 32–39, https://doi.org/10.1111/j.1445-2197.2010.05541.x.

[3] T. Peel, A. Cheng, K. Buising, P. Choong, Microbiological aetiology, epidemiology, and clinical profile of prosthetic joint infections: are current antibiotic prophylaxis guidelines effective? Antimicrob. Agents Chemother. 56 (5) (2012) 2386–2391, https://doi.org/10.1128/aac.06246-11.

[4] P. Sendi, F. Banderet, P. Graber, W. Zimmerli, Periprosthetic joint infection following Staphylococcus aureus bacteremia, J. Infect. 63 (1) (2011) 17–22, https://doi.org/10.1016/j.jinf.2011.05.005.

[5] J.W. Costerton, P.S. Stewart, E.P. Greenberg, Bacterial biofilms: a common cause of persistent infections, Science (New York, N.Y.) 284 (5418) (1999) 1318–1322, https://doi.org/10.1126/science.284.5418.1318.

[6] L.R. Hoffman, D.A. D'Argenio, M.J. MacCoss, Z. Zhang, R.A. Jones, S.I. Miller, Aminoglycoside antibiotics induce bacterial biofilm formation, Nature 436 (7054) (2005) 1171–1175, https://doi.org/10.1038/nature03912.

[7] C. Pangaud, M. Ollivier, J. Argenson, Outcome of single-stage versus two-stage exchange for revision knee arthroplasty for chronic periprosthetic infection, EFORT open reviews 4 (8) (2019) 495–502, https://doi.org/10.1302/2058-5241.4.190003.

[8] C. Wolf, N. Gu, J. Doctor, P. Manner, S. Leopold, Comparison of one and two-stage revision of total hip arthroplasty complicated by infection: a Markov expected-utility decision analysis, the Journal of bone and joint surgery, American volume 93 (7) (2011) 631–639, https://doi.org/10.2106/jbjs.I.01256.

[9] J. Cahill, B. Shadbolt, J. Scarvell, P. Smith, Quality of life after infection in total joint replacement, J. Orthop. Surg. 16 (1) (2008) 58–65, https://doi.org/10.1177/230949900801600115.

[10] J. Han, Y. Yang, J. Lu, C. Wang, Y. Xie, X. Zheng, Z. Yao, C. Zhang, Sustained release vancomycin-coated titanium alloy using a novel electrostatic dry powder coating technique may be a potential strategy to reduce implant-related infection, Bioscience trends 11 (3) (2017) 346–354, https://doi.org/10.5582/bst.2017.01061.

[11] Y. He, Y. Zhang, X. Shen, B. Tao, J. Liu, Z. Yuan, K. Cai, The fabrication and in vitro properties of antibacterial polydopamine-LL-37-POPC coatings on micro-arc oxidized titanium, Colloids Surf. B Biointerfaces 170 (2018) 54–63, https://doi.org/10.1016/j.colsurfb.2018.05.070.

[12] R. Chen, M. Willcox, K. Ho, D. Smyth, N. Kumar, Antimicrobial peptide melimine coating for titanium and its in vivo antibacterial activity in rodent subcutaneous infection models, Biomaterials 85 (2016) 142–151, https://doi.org/10.1016/j.biomaterials.2016.01.063.

[13] B. Huang, L. Tan, X. Liu, J. Li, S. Wu, A facile fabrication of novel stuff with antibacterial property and osteogenic promotion utilizing red phosphorus and near-infrared light, Bioact Mater 4 (1) (2019) 17–21, https://doi.org/10.1016/j.bioactmat.2018.11.002.

[14] X. Shen, Y. Zhang, P. Ma, L. Sutrisno, Z. Luo, Y. Hu, Y. Yu, B. Tao, C. Li, K. Cai, Fabrication of magnesium/zinc-metal organic framework on titanium implants to inhibit bacterial infection and promote bone regeneration, Biomaterials 212 (2019) 1–16, https://doi.org/10.1016/j.biomaterials.2019.05.008.

[15] S. Kunutsor, M. Whitehouse, J. Webb, A. Toms, I. Stockley, A. Taylor, S. Jones, M. Wilson, B. Burston, T. Board, J. Whittaker, A. Blom, A. Beswick, Re-infection outcomes following one- and two-stage surgical revision of infected hip prosthesis in unselected patients: protocol for a systematic review and an individual participant data meta-analysis, Syst. Rev. 4 (2015) 58, https://doi.org/10.1186/s13643-015-0044-0.

[16] U. Filipović, R.G. Dahmane, S. Ghannouchi, A. Zore, K. Bohinc, Bacterial adhesion on orthopedic implants, Adv. Colloid Interface Sci. 283 (2020) 102228, https://doi.org/10.1016/j.cis.2020.102228.

[17] L. Prodanov, E. Lamers, M. Domanski, R. Luttge, J.A. Jansen, X.F. Walboomers, The effect of nanometric surface texture on bone contact to titanium implants in rabbit tibia, Biomaterials 34 (12) (2013) 2920–2927, https://doi.org/10.1016/j.biomaterials.2013.01.027.

[18] E.G. Long, M. Buluk, M.B. Gallagher, J.M. Schneider, J.L. Brown, Human mesenchymal stem cell morphology, migration, and differentiation on micro and nano-textured titanium, Bioact Mater 4 (2019) 249–255, https://doi.org/10.1016/j.bioactmat.2019.08.001.

[19] A. Karthika, L. Kavitha, M. Surendiran, S. Kannan, D. Gopi, Fabrication of divalent ion substituted hydroxyapatite/gelatin nanocomposite coating on electron beam treated titanium: mechanical, anticorrosive, antibacterial and bioactive evaluations, RSC Adv. 5 (59) (2015) 47341–47352, https://doi.org/10.1039/c5ra05624a.

[20] D. Gopi, E. Shinyjoy, L. Kavitha, Influence of ionic substitution in improving the biological property of carbon nanotubes reinforced hydroxyapatite composite coating on titanium for orthopedic applications, Ceram. Int. 41 (4) (2015) 5454–5463, https://doi.org/10.1016/j.ceramint.2014.12.114.

[21] D. Gopi, A. Karthika, S. Nithiya, L. Kavitha, In vitro biological performance of minerals substituted hydroxyapatite coating by pulsed electrodeposition method, Mater. Chem. Phys. 144 (1–2) (2014) 75–85, https://doi.org/10.1016/j.matchemphys.2013.12.017.

[22] D. Stengel, K. Bauwens, J. Sehouli, A. Ekkernkamp, F. Porzsolt, Systematic review and meta-analysis of antibiotic therapy for bone and joint infections, the Lancet, Infectious diseases 1 (3) (2001) 175–188, https://doi.org/10.1016/s1473-3099(01)00094-9.

[23] M. Zilberman, J. Elsner, Antibiotic-eluting medical devices for various applications, J. Contr. Release 130 (3) (2008) 202–215, https://doi.org/10.1016/j.jconrel.2008.05.020.

[24] A. Bistolfi, G. Massazza, E. Verné, A. Massè, D. Deledda, S. Ferraris, M. Miola, F. Galetto, M. Crova, Antibiotic-loaded cement in orthopedic surgery: a review, ISRN orthopedics 2011 (2011) 290851, https://doi.org/10.5402/2011/290851.

[25] S. Gulhane, I.S. Vanhegan, F.S. Haddad, Single stage revision: regaining momentum, the Journal of bone and joint surgery, British 94 (2012) 120–122, https://doi.org/10.1302/0301-620x.94b11.30746.

[26] X. Wang, S. Liu, M. Li, P. Yu, X. Chu, L. Li, G. Tan, Y. Wang, X. Chen, Y. Zhang, C. Ning, The synergistic antibacterial activity and mechanism of multicomponent metal ions-containing aqueous solutions against Staphylococcus aureus, J. Inorg. Biochem. 163 (2016) 214–220, https://doi.org/10.1016/j.jinorgbio.2016.07.019.

[27] I. Yin, J. Zhang, I. Zhao, M. Mei, Q. Li, C. Chu, The antibacterial mechanism of silver nanoparticles and its application in dentistry, Int. J. Nanomed. 15 (2020) 2555–2562, https://doi.org/10.2147/ijn.S246764.

[28] A. El-Fiqi, N. Mandakhbayar, S.B. Jo, J.C. Knowles, J.H. Lee, H.W. Kim, Nanotherapeutics for regeneration of degenerated tissue infected by bacteria through the multiple delivery of bioactive ions and growth factor with antibacterial/angiogenic and osteogenic/odontogenic capacity, Bioact Mater 6 (1) (2021) 123–136, https://doi.org/10.1016/j.bioactmat.2020.07.010.

[29] K.M. Reddy, K. Feris, J. Bell, D.G. Wingett, C. Hanley, A. Punnoose, Selective toxicity of zinc oxide nanoparticles to prokaryotic and eukaryotic systems, Appl. Phys. Lett. 90 (2007) 2139021–2139023, https://doi.org/10.1063/1.2742324, 213902.

[30] D. Widyaratih, P. Hagedoorn, L. Otten, M. Ganjian, N. Tümer, I. Apachitei, C. Hagen, L. Fratila-Apachitei, A. Zadpoor, Towards osteogenic and bactericidal nanopatterns? Nanotechnology 30 (20) (2019) 20LT01, https://doi.org/10.1088/1361-6528/ab0a3a.

[31] J. Jenkins, J. Mantell, C. Neal, A. Gholinia, P. Verkade, A. Nobbs, B. Su, Antibacterial effects of nanopillar surfaces are mediated by cell impedance, penetration and induction of oxidative stress, Nat. Commun. 11 (1) (2020) 1626, https://doi.org/10.1038/s41467-020-15471-x.

[32] S. Park, H. Park, K. Sun, Y. Gwon, M. Seong, S. Kim, T. Park, H. Hyun, Y. Choung, J. Kim, H. Jeong, Hydrogel nanospike patch as a flexible anti-pathogenic scaffold for regulating stem cell behavior, ACS Nano 13 (10) (2019) 11181–11193, https://doi.org/10.1021/acsnano.9b04109.

[33] S. Pogodin, J. Hasan, V. Baulin, H. Webb, V. Truong, T. Phong Nguyen, V. Boshkovikj, C. Fluke, G. Watson, J. Watson, R. Crawford, E. Ivanova, Biophysical model of bacterial cell interactions with nanopatterned cicada wing surfaces, Biophys. J. 104 (4) (2013) 835–840, https://doi.org/10.1016/j.bpj.2012.12.046.

[34] E. Ivanova, J. Hasan, H. Webb, G. Gervinskas, S. Juodkazis, V. Truong, A. Wu, R. Lamb, V. Baulin, G. Watson, J. Watson, D. Mainwaring, R. Crawford, Bactericidal activity of black silicon, Nat. Commun. 4 (2013) 2838, https://doi.org/10.1038/ncomms3838.

[35] M.B. Sedelnikova, E.G. Komarova, Y.P. Sharkeev, T.V. Tolkacheva, I.A. Khlusov, L. S. Litvinova, K.A. Yurova, V.V. Shupletsova, Comparative investigations of structure and properties of micro-arc wollastonite-calcium phosphate coatings on titanium and zirconium-niobium alloy, Bioact Mater 2 (3) (2017) 177–184, https://doi.org/10.1016/j.bioactmat.2017.01.002.

[36] H. Liu, M. Lin, X. Liu, Y. Zhang, Y. Luo, Y. Pang, H. Chen, D. Zhu, X. Zhong, S. Ma, Y. Zhao, Q. Yang, X. Zhang, Doping bioactive elements into a collagen scaffold based on synchronous self-assembly/mineralization for bone tissue engineering, Bioact Mater 5 (4) (2020) 844–858, https://doi.org/10.1016/j.bioactmat.2020.06.005.

[37] S. Yao, B. Jin, Z. Liu, C. Shao, R. Zhao, X. Wang, R. Tang, Biomineralization: from material tactics to biological strategy, advanced materials (deerfield beach, fla, 29 (14), http://doi.org/10.1002/adma.201605903, 2017.

[38] J. Inzana, E. Schwarz, S. Kates, H. Awad, Biomaterials approaches to treating implant-associated osteomyelitis, Biomaterials 81 (2016) 58–71, https://doi.org/10.1016/j.biomaterials.2015.12.012.

[39] G. Wang, W. Jiang, S. Mo, L. Xie, Q. Liao, L. Hu, Q. Ruan, K. Tang, B. Mehrjou, M. Liu, L. Tong, H. Wang, J. Zhuang, G. Wu, P. Chu, Nonleaching antibacterial concept demonstrated by in situ construction of 2D nanoflakes on magnesium, Advanced science (Weinheim, Baden-Wurttemberg, Germany) 7 (1) (2020) 1902089, https://doi.org/10.1002/advs.201902089.

[40] J. Thompson, R. Miller, A. Ashbaugh, C. Dillen, J. Pickett, Y. Wang, R. Ortines, R. Sterling, K. Francis, N. Bernthal, T. Cohen, C. Tkaczyk, L. Yu, C. Stover, A. DiGiandomenico, B. Sellman, D. Thorek, L. Miller, Mouse model of Gram-negative prosthetic joint infection reveals therapeutic targets, JCI insight 3 (17) (2018), https://doi.org/10.1172/jci.insight.121737.

[41] N. Ren, J. Li, J. Qiu, Y. Sang, H. Jiang, R. Boughton, L. Huang, W. Huang, H. Liu, Nanostructured titanate with different metal ions on the surface of metallic titanium: a facile approach for regulation of rBMSCs fate on titanium implants, Small 10 (15) (2014) 3169–3180, https://doi.org/10.1002/smll.201303391.

[42] S. Yamaguchi, S. Nath, T. Matsushita, T. Kokubo, Controlled release of strontium ions from a bioactive Ti metal with a Ca-enriched surface layer, Acta Biomater. 10 (5) (2014) 2282–2289, https://doi.org/10.1016/j.actbio.2014.01.026.

[43] C. Yang, Y. Liu, M. Yan, Bond strength of ceramics heat-pressed onto three dental alloys, J. Prosthet. Dent 121 (5) (2019) 867, https://doi.org/10.1016/j.prosdent.2019.02.018, e1-867.e5.

[44] M. Lorenzetti, I. Dogša, T. Stošicki, D. Stopar, M. Kalin, S. Kobe, S. Novak, The influence of surface modification on bacterial adhesion to titanium-based substrates, ACS Appl. Mater. Interfaces 7 (3) (2015) 1644–1651, https://doi.org/10.1021/am507148n.

[45] K. Baskar, T. Anusuya, G. Devanand Venkatasubbu, Mechanistic investigation on microbial toxicity of nano hydroxyapatite on implant associated pathogens, Materials science & engineering. C, Materials for biological applications 73 (2017) 8–14, https://doi.org/10.1016/j.msec.2016.12.060.

[46] F. Zou, H. Zhou, D.Y. Jeong, J. Kwon, S.U. Eom, T.J. Park, S.W. Hong, J. Lee, Wrinkled surface-mediated antibacterial activity of graphene oxide nanosheets,

ACS Appl. Mater. Interfaces 9 (2) (2017) 1343–1351, https://doi.org/10.1021/acsami.6b15085.
[47] V. Uskoković, S. Tang, M. Nikolić, S. Marković, V. Wu, Calcium phosphate nanoparticles as intrinsic inorganic antimicrobials: in search of the key particle property, Biointerphases 14 (3) (2019), 031001, https://doi.org/10.1116/1.5090396.
[48] D.P. Linklater, V.A. Baulin, S. Juodkazis, R.J. Crawford, P. Stoodley, E.P. Ivanova, Mechano-bactericidal actions of nanostructured surfaces, Nat. Rev. Microbiol. (2020), https://doi.org/10.1038/s41579-020-0414-z.
[49] I.A. Khlusov, Y. Dekhtyar, Y.P. Sharkeev, V.F. Pichugin, M.Y. Khlusova, N. Polyaka, F. Tyulkin, V. Vendinya, E.V. Legostaeva, L.S. Litvinova, V.V. Shupletsova, O. G. Khaziakhmatova, K.A. Yurova, K.A. Prosolov, Nanoscale electrical potential and roughness of a calcium phosphate surface promotes the osteogenic phenotype of stromal cells, Materials 11 (6) (2018), https://doi.org/10.3390/ma11060978.
[50] D. Kovačević, R. Pratnekar, K. Godič Torkar, J. Salopek, G. Dražić, A. Abram, K. Bohinc, Influence of polyelectrolyte multilayer properties on bacterial adhesion capacity, Polymers 8 (10) (2016), https://doi.org/10.3390/polym8100345.
[51] B. Li, B.E. Logan, Bacterial adhesion to glass and metal-oxide surfaces, Colloids Surf. B Biointerfaces 36 (2) (2004) 81–90, https://doi.org/10.1016/j.colsurfb.2004.05.006.
[52] H.M. Kim, T. Himeno, T. Kokubo, T. Nakamura, Process and kinetics of bonelike apatite formation on sintered hydroxyapatite in a simulated body fluid, Biomaterials 26 (21) (2005) 4366–4373, https://doi.org/10.1016/j.biomaterials.2004.11.022.
[53] C. Arciola, D. Campoccia, L. Montanaro, Implant infections: adhesion, biofilm formation and immune evasion, Nature reviews, Microbiology 16 (7) (2018) 397–409, https://doi.org/10.1038/s41579-018-0019-y.
[54] A. Sirelkhatim, S. Mahmud, A. Seeni, N.H.M. Kaus, L.C. Ann, S.K.M. Bakhori, H. Hasan, D. Mohamad, Review on zinc oxide nanoparticles: antibacterial activity and toxicity mechanism, Nano-Micro Lett. 7 (3) (2015) 219–242, https://doi.org/10.1007/s40820-015-0040-x.
[55] J. Li, L. Tan, X. Liu, Z. Cui, X. Yang, K.W.K. Yeung, P.K. Chu, S. Wu, Balancing bacteria-osteoblast competition through selective physical puncture and biofunctionalization of ZnO/Polydopamine/Arginine-Glycine-Aspartic acid-cysteine nanorods, ACS Nano 11 (11) (2017) 11250–11263, https://doi.org/10.1021/acsnano.7b05620.
[56] S. Lischer, E. Körner, D. Balazs, D. Shen, P. Wick, K. Grieder, D. Haas, M. Heuberger, D. Hegemann, Antibacterial burst-release from minimal Ag-containing plasma polymer coatings, J. R. Soc. Interface 8 (60) (2011) 1019–1030, https://doi.org/10.1098/rsif.2010.0596.
[57] A. Trampuz, A. Widmer, Infections associated with orthopedic implants, Curr. Opin. Infect. Dis. 19 (4) (2006) 349–356, https://doi.org/10.1097/01.qco.0000235161.85925.e8.
[58] A. Tande, R. Patel, Prosthetic joint infection, Clin. Microbiol. Rev. 27 (2) (2014) 302–345, https://doi.org/10.1128/cmr.00111-13.
[59] R. Lynch, R. Duckworth, Chapter 4: microelements: Part I: Zn, Sn, Cu, Fe and I, Monogr. Oral Sci. 28 (2020) 32–47, https://doi.org/10.1159/000499007.
[60] A. Overmann, C. Aparicio, J. Richards, I. Mutreja, N. Fischer, S. Wade, B. Potter, T. Davis, J. Bechtold, J. Forsberg, D. Dey, Orthopaedic osseointegration: implantology and future directions, J. Orthop. Res. : official publication of the Orthopaedic Research Society 38 (7) (2020) 1445–1454, https://doi.org/10.1002/jor.24576.
[61] S. Goodman, Z. Yao, M. Keeney, F. Yang, The future of biologic coatings for orthopaedic implants, Biomaterials 34 (13) (2013) 3174–3183, https://doi.org/10.1016/j.biomaterials.2013.01.074.
[62] N. Shah, M. Hyder, J. Moskowitz, M. Quadir, S. Morton, H. Seeherman, R. Padera, M. Spector, P. Hammond, Surface-mediated bone tissue morphogenesis from tunable nanolayered implant coatings, Sci. Transl. Med. 5 (191) (2013) 191ra83, https://doi.org/10.1126/scitranslmed.3005576.
[63] A. Overmann, J. Forsberg, The state of the art of osseointegration for limb prosthesis, Biomedical engineering letters 10 (1) (2020) 5–16, https://doi.org/10.1007/s13534-019-00133-9.
[64] M. Schumacher, M. Gelinsky, Strontium modified calcium phosphate cements - approaches towards targeted stimulation of bone turnover, J. Mater. Chem. B 3 (23) (2015) 4626–4640, https://doi.org/10.1039/c5tb00654f.
[65] Z. Saidak, P. Marie, Strontium signaling: molecular mechanisms and therapeutic implications in osteoporosis, Pharmacol. Ther. 136 (2) (2012) 216–226, https://doi.org/10.1016/j.pharmthera.2012.07.009.
[66] S. Kini, A. Gabr, R. Das, M. Sukeik, F. Haddad, Two-stage revision for periprosthetic hip and knee joint infections, Open Orthop. J. 10 (2016) 579–588, https://doi.org/10.2174/1874325001610010579.
[67] F. Rowan, M. Donaldson, J. Pietrzak, F. Haddad, The role of one-stage exchange for prosthetic joint infection, Current reviews in musculoskeletal medicine 11 (3) (2018) 370–379, https://doi.org/10.1007/s12178-018-9499-7.